



Reconstruction, rumpling, and Dirac states at the (001) surface of the topological crystalline insulator $\text{Pb}_{1-x}\text{Sn}_x\text{Se}$

A. Łusakowski  and P. Bogusławski 

Institute of Physics, Polish Academy of Sciences, Aleja Lotników 32/46, PL-02-668 Warsaw, Poland

T. Story 

*Institute of Physics, Polish Academy of Sciences, Aleja Lotników 32/46, PL-02-668 Warsaw, Poland
and International Research Centre MagTop, Institute of Physics, PAS, Aleja Lotników 32/46, PL-02-668, Warsaw, Poland*



(Received 19 April 2023; revised 10 July 2023; accepted 16 August 2023; published 5 September 2023)

The equilibrium atomic configuration and electronic structure of the (001) surface of the IV-VI semiconductors PbTe, PbSe, SnTe, and SnSe are studied using density functional theory methods. At the surfaces of all these compounds, the displacements of ions from their perfect lattice sites reveal two features characteristic of rocksalt crystals. First, the ionic displacements occur only along the direction perpendicular to the surface, and they exhibit a rumpling effect; that is, the vertical shifts of cations and anions differ. Second, the interlayer spacing of the first few monolayers at the surface oscillates. Our results are in good agreement with previous x-ray experimental data and theoretical results where available. They are also consistent with the presence of two {110} mirror planes at the (001) surface of the rocksalt. On the other hand, experiments performed for the topological $\text{Pb}_{1-x}\text{Sn}_x\text{Se}$ alloy indicate breaking of the mirror symmetry due to a large 0.3 Å relative displacement of the cation and anion sublattices at the surface, which induces the opening of the gap of the Dirac cones. Our results for $\text{Pb}_{1-x}\text{Sn}_x\text{Se}$, including simulated scanning tunneling microscopy images, are in contradiction to these findings since surface reconstructions with broken symmetry are never ground state configurations. The impact of the theoretically determined surface configurations and of the chemical disorder on the surface states is analyzed.

DOI: [10.1103/PhysRevB.108.125201](https://doi.org/10.1103/PhysRevB.108.125201)

I. INTRODUCTION

Various propositions envisioned for applications of topological materials rely on control of their electronic structure. This issue is motivating considerable ongoing experimental and theoretical research. As has been demonstrated, properties of topological electron states can be tuned by gate voltage, crystal strain, magnetic field, or magnetization. This includes, in particular, the opening of the energy gap in the otherwise metallic Dirac-like spectrum.

In the case of the IV-VI narrow-gap semiconductors $\text{Pb}_{1-x}\text{Sn}_x\text{Te}$ and $\text{Pb}_{1-x}\text{Sn}_x\text{Se}$ studied here, it is possible to observe a transition from a normal insulator (NI) to a topological crystalline insulator (TCI) phase by changing chemical composition, external pressure, or temperature. Those materials crystallize in the rocksalt (RS) structure [1,2]. The key physical factor responsible for the existence of the nontrivial topological phase is not the time reversal symmetry, as is the case in the well-known topological insulator $(\text{Bi,Sb})_2(\text{Te,Se})_3$, but the mirror symmetry with respect to the {110} crystallographic planes [3–6]. This symmetry warrants the existence of zero-gap Dirac-like states on certain high-symmetry crystal facets of TCI crystals, such as (001), (111), and (110).

Scanning tunneling microscopy and spectroscopy (STM/STS) and Landau level spectroscopy (LLS) experiments suggested that at the (001) surface of $\text{Pb}_{1-x}\text{Sn}_x\text{Se}$ the anion and cation sublattices are displaced with respect to each other along the [110] direction [7,8]. Such displacement preserves the mirror symmetry with respect to the (110) plane

but breaks the symmetry with respect to the $(\bar{1}10)$ plane. This symmetry breaking gives rise to the opening of the gap in two out of a total of four valleys of surface Dirac TCI states located near the \bar{X} points of the surface Brillouin zone (projections of four bulk L points) on the $\bar{\Gamma}$ - \bar{X} lines. The results of STS/LLS studies in magnetic field [7] confirmed the conclusion that two kinds of surface states coexist, those with a vanishing energy gap and those with a finite one. In a subsequent paper [8] the STM images directly showed a relative displacement of sublattices of about 0.3 Å. In both papers, only the low-temperature measurements were reported. This problem was also studied experimentally in Ref. [9] using angle-resolved photoemission spectroscopy (ARPES), a technique able to selectively study different valleys in k space. Importantly, the analysis included samples with different Sn concentrations and was performed at different temperatures. In agreement with Refs. [7,8], at low temperatures two kinds of surface states were observed: gapless and with an energy gap of the order of 25 meV [9]. The surface energy gap decreased with increasing temperature, and depending on x , it disappeared in the temperature range of 100–200 K, as expected from the topological T - x phase diagram of $\text{Pb}_{1-x}\text{Sn}_x\text{Se}$ [10]. In Refs. [7–9] the mechanism of symmetry breaking at the surface of bulk crystals with perfect cubic symmetry was not proposed. Instead, the effect was tentatively ascribed to the tendency of the IV-VI crystals to transition from the cubic to rhombohedral phase observed in the tellurides SnTe, GeTe, and $\text{Pb}_{1-x}\text{Sn}_x\text{Te}$ [1,2].

The surface reconstruction proposed in [8] is unexpected. This is because previous theoretical and experimental works on {001} surfaces of compounds crystallizing in the rock-salt structure [11–17] revealed that in all cases considerable displacements from the ideal bulk sites take place, but their character is in qualitative disagreement with that found in [8]. In particular, three features universally characterize surface equilibrium geometries [11–17]. First, atomic displacements occur in only the z direction (perpendicular to the surface); thus, both the ideal RS surface periodicity and symmetry are maintained. Second, the top surface layer is not ideally flat because cations and anions shift by different amounts in the z direction; this effect is referred to as rumpling. Third, the average interlayer spacings relative to the ideal bulk geometry are modified, and the distance between the first and the second layers is reduced, while that between the second and third layers is increased compared to the ideal bulk value. This oscillatory behavior occurs for the first few subsurface atomic layers. No (110) mirror plane symmetry breaking reconstructions were found. Sawada and Nakamura [15] summarized early works and used the Verwey model [17] to show that the relaxations are largely determined by electrostatics. In fact, both long-range electric fields and different atomic polarizabilities of cations and anions are responsible for the effects above.

Results for $\text{Pb}_{1-x}\text{Sn}_x\text{Te}$ are contradictory as well. Yan *et al.* [18] studied the band structure of $\text{Pb}_{1-x}\text{Sn}_x\text{Te}(111)$ overlayers in the full composition range. The Dirac states were seen by ARPES also for the TCI SnTe, and neither band gap nor crystal structure anomalies were noticed. On the other hand, recently, a symmetry breaking analogous to that in $\text{Pb}_{1-x}\text{Sn}_x\text{Se}$ was also observed [19].

Here, we theoretically study the ground state atomic configurations and the electronic structure of the (001) surfaces of some semiconductors from the IV-VI family. Of particular interest are the possible mechanisms of symmetry breaking and the gap opening in surface states. This paper is organized as follows. In Sec. II we present details of the *ab initio* calculations, together with the method for obtaining the tight-binding approximation (TBA) Hamiltonian from the *ab initio* results. Section III is devoted to the geometric optimization of the considered systems. Our results are in full accord with previous findings [11–17] regarding the features of the surface geometry of the RS crystals listed above but do not confirm the surface reconstruction proposed in Ref. [8]. Additional insight is obtained from our simple simulations of the STM images. Finally, electron dispersion relations of the surface states are provided, where we also study the influence of both surface deformations and chemical disorder on the band gap. This allows us to determine how a realistic atomic-scale surface morphology of the crystal facets hosting topological states influences electronic spectrum. We identify the conditions under which the Dirac-cone-like metallic spectrum can be shifted in k space along specific directions or can exhibit an about 1–10 meV gap opening effect relevant for, e.g., far-infrared and terahertz applications. Section IV concludes the paper.

II. METHODS OF CALCULATIONS

The properties of layers are analyzed using slabs with identical top and bottom layers and thus with an odd number

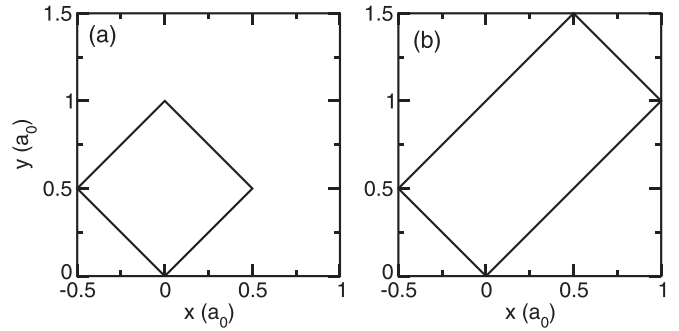


FIG. 1. Surface unit cells for the (a) SC1 and SC2 (b) supercells (see text).

of monolayers. The slabs are separated by 10 \AA of vacuum. For pure compounds supercell SC1 is defined by the vectors $\mathbf{a}_1 = a_0(\frac{1}{2}, \frac{1}{2}, 0)$, $\mathbf{a}_2 = a_0(-\frac{1}{2}, \frac{1}{2}, 0)$, and $\mathbf{a}_3 = a_0(0, 0, n_h + \frac{1}{2})$, where $2n_h + 1$ is the number of monolayers in the slab. The surface unit cell contains one cation and one anion. For mixed crystals, when we want to take into account the symmetry breaking due to chemical disorder, we use larger supercells (labeled SC2) based on the vectors $\mathbf{a}_1 = a_0(1, 1, 0)$, $\mathbf{a}_2 = a_0(-\frac{1}{2}, \frac{1}{2}, 0)$, and $\mathbf{a}_3 = a_0(0, 0, n_h + \frac{1}{2})$. Supercell SC2 consists of two SC1 supercells, which enables an easy presentation of dispersion relations. The surface unit cells of SC1 and SC2 are shown in Fig. 1.

The density functional theory (DFT) calculations are performed using the OpenMX package [20]. They are based on the local density approximation [21] and the exchange-correlation functional of Ref. [22]. Summations over the Brillouin zone are performed by applying a $4 \times 4 \times 1$ mesh, with the convergence check using a $8 \times 8 \times 1$ mesh for SC1 and a $4 \times 8 \times 1$ mesh for SC2. Atomic pseudopotentials for Pb and Te were described in Ref. [23], and those for Sn and Se were taken from OpenMX. Atomic relaxations in the first five surface layers are taken into account. The calculations were stopped when the forces acting on atoms were smaller than 10^{-4} hartrees/bohr, and total energy was converged to within 10^{-6} hartrees.

The calculated equilibrium RS lattice parameters a_0 are 6.42 \AA for PbTe, 6.40 \AA for SnTe, and 6.14 \AA for PbSe. These values are slightly different from the respective experimental ones, which are 6.46 , 6.30 , and 6.12 \AA , respectively. The experimental value for RS-SnSe is not known since SnSe in the RS structure is unstable; our calculations result in 6.10 \AA for RS-SnSe. Using the theoretical lattice parameters, we optimize surface geometry for 11 and 23 monolayer (ML) thick slabs, and the equilibrium atomic positions are practically identical.

Reliable calculations of the dispersion relations of surface states require sufficiently thick slabs. Otherwise, the relevant surface states localized at the top and bottom surfaces interact, which leads to a hybridization-driven opening of energy gaps in the spectrum of the surface states. Our convergence checks indicate that the coupling between the two surfaces is negligibly small for slabs with a thickness of about 150 ML, in agreement with Ref. [18]. This corresponds to about 600 atoms in the supercell, and thus, the *ab initio* calculations, although, in principle, possible, are not practical.

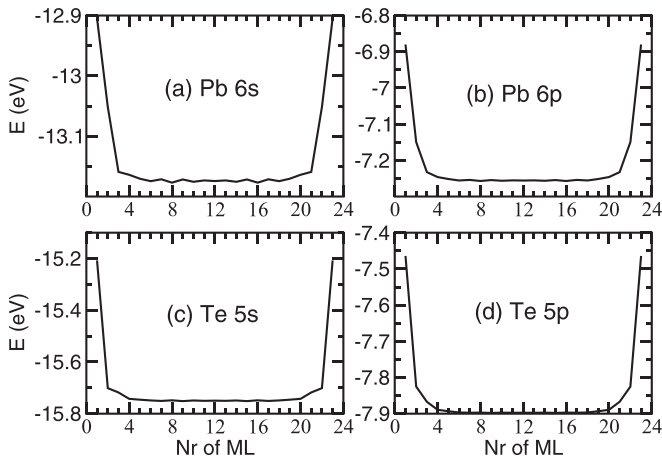


FIG. 2. Calculated dependence of the TBA parameters, namely, the energies of the $6s$ (Pb), $6p$ (Pb), $5s$ (Te), and $5p$ (Te) orbitals, on the atomic position in the 23-ML slab.

An efficient alternative to apply is the TBA approach based on the local density approximation results. This requires knowledge of the TBA parameters, and they are provided by the OpenMX code. Here, we use the TBA parameters determined by *ab initio* calculations for 23 ML thick slabs. In the slab geometry, an issue to solve is that the TBA parameters for a given atomic species (e.g., Pb in PbTe) depend on the ion's position in the slab. Indeed, because the local coordination of a Pb ion at the PbTe surface is not the same as in the bulk, the parameters of Pb near the surface differ from those in the bulk, and this difference depends on the distance from the slab's surfaces. This also holds in the case of the interatomic TBA parameters. According to our results, significant variations of the parameters are limited to the 4 ML closest to the surfaces. This important fact has typically been ignored in the literature.

As an example, in Fig. 2 we show the dependence of the TBA energies of the s and p orbitals of both Pb and Te ions on their positions in the PbTe slab. Energy differences between the values in the bulk and in the outermost surface layer are 0.3 eV for the Pb orbitals and somewhat larger, about 0.5 eV, for the Te orbitals. The dependence of the Mulliken charge on atomic positions in the slab, shown in Fig. 3, reveals the same feature: their significant variations are limited to the first four layers. The difference in the values for the first ML and at the slab center is not very large, of the order of 2%. Similar differences are found for other TBA parameters and for the remaining crystals. Importantly, however, these variations have a critical impact on the energy dispersion relations and the character of the surface states. This is illustrated in Fig. 4, which presents the dispersion relations for a 123 ML thick slab of PbTe along the $\bar{\Gamma} \rightarrow \bar{X}$ and $\bar{X} \rightarrow \bar{M}$ directions obtained within the TBA. Only the highest 25 valence states and the lowest 25 conduction states are displayed. The bulk lattice parameter $a_0 = 6.20$ Å is assumed, for which PbTe is in the nontrivial topological state [24]. The results in Fig. 4(a) are obtained with all TBA parameters equal to the TBA parameters of bulk PbTe. In the case of Fig. 4(b), the TBA parameters are position dependent and determined according to the procedure described below. We expect that the highest occupied levels should be the surface states, and indeed, this

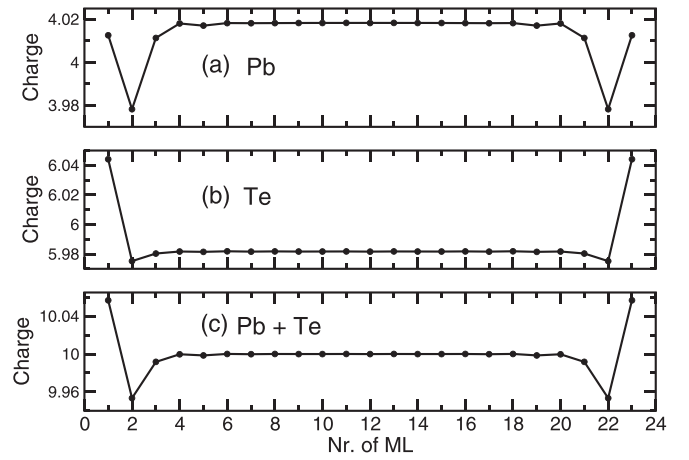


FIG. 3. Dependence of Mulliken charges on the atom positions in the 23-ML slab: (a) Pb, (b) Te, and (c) the sum of (a) and (b).

situation is observed with a well-defined Dirac cross [see Fig. 4(b)]. In contrast, in the case in Fig. 4(a) a number of bands are above the energy of the highest occupied band and certainly cannot be classified as conduction bands. We conclude therefore that the position dependence of the TBA parameters close to the surface must be taken into account, and this is one of important messages of our work.

The position-dependent TBA parameters for thick layers are obtained as follows. We begin with *ab initio* calculations for an easy to handle 23 ML slab with equivalent top and bottom surfaces. The slab is partitioned into three regions, the (I) bottom, (II) internal, and (III) top regions, containing 6, 10, and 7 ML, respectively. The corresponding TBA parameters are given in the output of the *ab initio* calculations. The

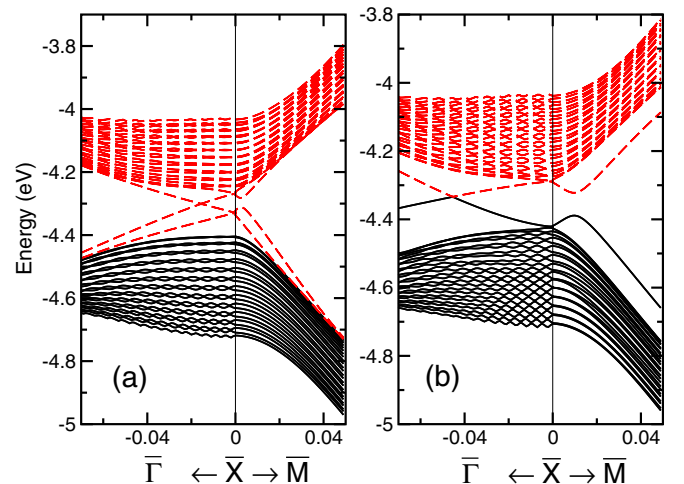


FIG. 4. Dispersion relations along the $\bar{X} \rightarrow \bar{\Gamma}$ and $\bar{X} \rightarrow \bar{M}$ directions of the 25 highest valence (black lines) and the 25 lowest conduction (red broken lines) bands for a 123 monolayer thick slab of PbTe with the lattice parameter $a_0 = 6.20$ Å. (a) The TBA parameters are independent of the position in the slab, and (b) the TBA parameters are position dependent (see text). The wave vector on the x axis along both the $\bar{X} \rightarrow \bar{\Gamma}$ and $\bar{X} \rightarrow \bar{M}$ directions is in units of $2\sqrt{2}\pi/a_0$.

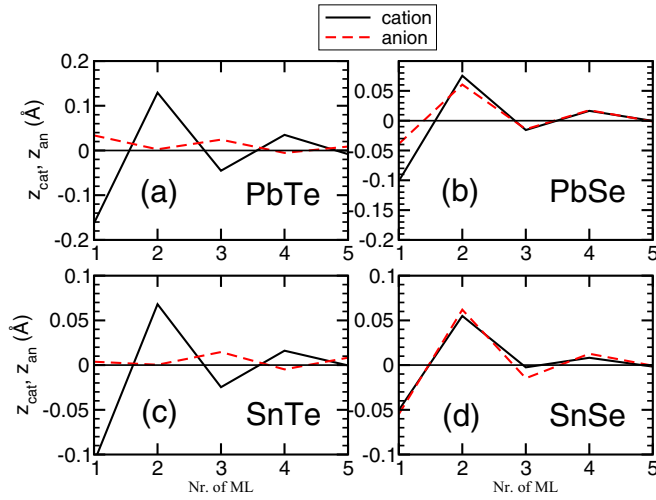


FIG. 5. Displacements of cations and anions from the ideal rock-salt sites in the first 5 ML for (a) PbTe, (b) PbSe, (c) SnTe, and (d) SnSe.

assumed thickness of the outer regions, I and III, guarantees that all surface effects are contained therein, and thus, the internal region, region II, correctly reproduces the bulk. In particular, in our TBA method the interatomic couplings extend to the third neighbor of a given atom, and the atomic relaxations along with the effects of the nonbulk coordinations at the surface extend to the first 4 ML (see Figs. 2 and 3). The TBA parameters for the internal region, region II, are those for bulk crystals. For thicker slabs three regions are also considered. The first and last regions contain 6 and 7 ML, respectively, and the internal region is a certain number of repetitions of region II of the 23 ML slab. For these three regions the TBA parameters are taken from regions I, II, and III of a 23 thick ML slab, respectively.

III. ATOMIC CONFIGURATIONS AND THE ELECTRONIC STRUCTURE OF (001) SURFACES

A. Ground state atomic configurations

The atomic configuration at a (001) surface of a rocksalt crystal can be defined by two parameters [12], namely, the average z coordinate of the i th layer $z(i) = [z_{\text{cat}}(i) + z_{\text{an}}(i)]/2$ and the rumpling parameter of that layer $r(i) = [z_{\text{an}}(i) - z_{\text{cat}}(i)]/d_0$. Here, d_0 is the equilibrium bond length, and the z coordinate of cations (anions) from the i th layer with respect to perfect positions is denoted by $z_{\text{cat}}(i)$ [$z_{\text{an}}(i)$], with $i = 1$ being the surface. The change in the interlayer spacing between layers i and $i + 1$ is $\delta_{i,i+1} = [z(i+1) - z(i)]/d_0$. To find the ground state atomic configurations, three initial geometries are considered. In the first one, all atoms are at the ideal rock-salt sites. In the remaining cases, the initial displacements for Te atoms are limited to only the surface layer and amount to (0.3, 0.3, 0) and (0.4, 0.2, -0.1) Å, respectively. These choices are meant to initiate the surface configuration suggested in Ref. [8], which breaks the surface symmetry.

We first consider ionic relaxations perpendicular to the surface. The calculated final displacements $z(i)$ along the z axis do not depend on the initial configuration and are shown in Fig. 5 for all the considered compounds. Next, both the

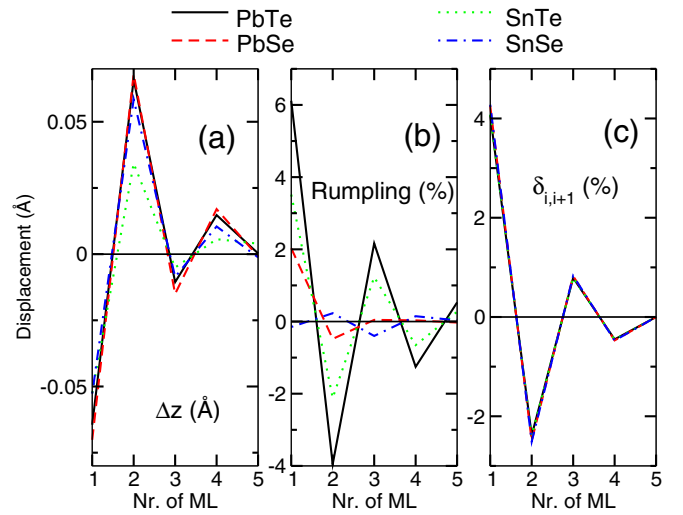


FIG. 6. Changes in (a) the average z coordinates of the monolayers, (b) rumpling r , and (c) the interlayer spacings δ for first 5 ML of PbTe, PbSe, SnTe, and SnSe. Note that the calculated δ are practically identical for all the considered crystals.

rumpling and the interlayer spacing are presented in detail in Fig. 6. For PbTe and PbSe, these parameters were calculated previously [11,12,16]. There are some differences between our values and those presented in the literature, but the qualitative picture is the same.

The PbTe(001) surface was experimentally investigated in detail. Low-energy electron diffraction measurements performed in Ref. [11] revealed a large rumpling, $r(1) = 6.8\%$, which corresponds to displacements of about 0.2 Å. Next, the measured interlayer spacings exhibit an oscillatory behavior, with $\delta_{1,2} = 4\%$ and $\delta_{2,3} = -2\%$. Our results shown in Fig. 6 are in good agreement with these data: the rumpling of the first layer is $r(1) \approx 6\%$, and the changes in interlayer spacings are $\delta_{1,2} \approx 4\%$ and $\delta_{2,3} \approx -2\%$. Previous first-principles calculations for PbTe(001) [11,12,16] found the rumpling somewhat lower than that observed, but they confirmed the outward (inward) shift of Te (Pb) ions. Next, the calculated interlayer spacings exhibited an oscillatory behavior with values close to those measured.

Rumpling in the PbX series depends on the anion. Indeed, in contrast to PbTe(001), a very small rumpling at the PbS(001) surface was observed [25]. Theoretical results of Refs. [12,13,16] are in good agreement with experiment. Interestingly, rumpling at the PbS(001) and PbTe(001) surfaces is opposite since in the former case the S anions exhibit a small *inward* displacement. According to Figs. 5 and 6, relaxations at PbSe(001) are intermediate between those for PbS(001) and PbTe(001). In particular, the rumpling at PbSe(001) is smaller than that for PbTe as it amounts to 2%. This confirms the results of Ref. [13]. The interlayer spacing exhibits the typical oscillatory behavior.

The results obtained for RS-SnSe and RS-SnTe are presented in Figs. 5 and 6, respectively. As we see, the z displacements of the consecutive layers are similar for all systems, and the interlayer distances always oscillate. Also, the rumpling oscillates, changing the sign for adjacent layers, but it is more pronounced in the tellurides than in the selenides.

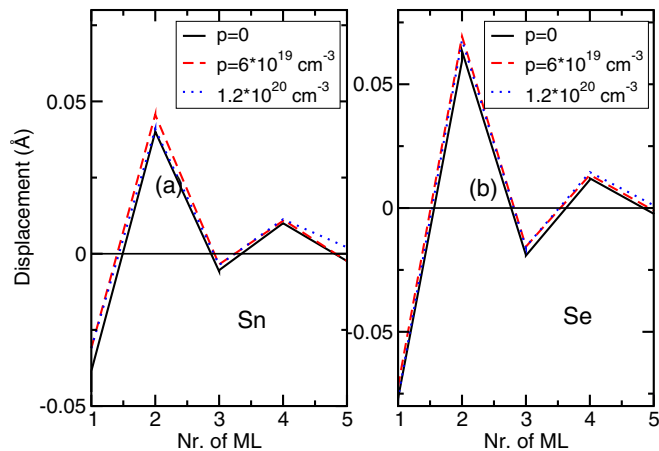


FIG. 7. Displacements of atoms in the first monolayers of SnSe along the [001] direction with respect to the positions in the perfect rocksalt lattice after the geometric optimization as a function of the hole concentration p . The results for (a) Sn and (b) Se are shown.

We recall here that the RS phase of SnSe is only metastable; nevertheless, surface properties of RS-SnSe(001) are expected and found to be similar to those of other members of the RS-IV-VI family.

Equilibrium atomic configurations can depend on the presence of free carriers. Indeed, it is well known that Sn-based IV-VI compounds typically are highly p type due to the presence of high concentrations of electrically active cation vacancies. This is also the case for crystals investigated in Ref. [8]. There are two possible consequences of this fact. First, charge transfer processes taking place at the surface (see Fig. 3) can be screened and/or affected by the presence of free carriers in the layer. This, in turn, can influence the surface geometry. Second, bulk SnTe assumes the NaCl structure at higher temperatures, and with decreasing temperature a transition to the rhombohedral phase takes place. However, this transition is suppressed by concentrations of holes higher than $1.3 \times 10^{21} \text{ cm}^{-3}$ [26]. (This transition also becomes suppressed with the increasing content of Pb in $\text{Pb}_{1-x}\text{Sn}_x\text{Te}$.) Accordingly, the recent experiment of Wei *et al.* [27] suggested that strongly anomalous transport features observed in PbTe/SnTe heterostructures originate in the free-carrier-driven symmetry breaking in SnTe layers caused by the above-mentioned varying hole densities.

The results above motivated us to analyze the impact of free carriers on atomic displacements. The OpenMX package allows performing calculations for nonzero concentrations of free carriers. The calculations were done for free-carrier concentrations between 10^{20} cm^{-3} holes and 10^{20} cm^{-3} electrons, and the results are shown in Fig. 7. While the relaxation energies (i.e., the energy gains induced by the relaxation from the ideal to the equilibrium configuration) are dependent on carrier concentration to some extent, the final geometries are highly nonsensitive to the presence of free carriers. In all cases, the ionic displacements in the (001) plane are negligibly small. The presence of $1.2 \times 10^{20} \text{ cm}^{-3}$ electrons induces ionic displacements of about 0.01 \AA . The same amount of holes induces a similar change, but of opposite sign.

We now turn to the displacements in the (x, y) plane. When the ideal RS configuration is used as input, the final ionic displacements in the (x, y) plane always vanish for all the considered crystals. Using the symmetry breaking initial configurations leads to a final configuration with small displacements of about $|0.03| \text{ \AA}$. We ascribe this result to the finite accuracy of our calculations since in all cases the total energy of the symmetry breaking configurations is higher by about $0.5 \text{ meV}/(\text{surface atom})$ compared with that of the symmetric ground state.

In conclusion, our results do not confirm the presence of symmetry breaking in the (x, y) plane at the surface which was proposed in Ref. [8] based on the STM measurements. In fact, our study indicates instability of those configurations. Also, the presence of free carriers can be ruled out as a cause of the surface reconstruction reported in Ref. [8]. Independent experiments, in particular STM, are needed to clarify the situation.

B. Simulation of STM images

Conclusions reported in Ref. [8] regarding the surface geometry are based on the STM measurements. In those measurements the local density of states near the surface plays the main role [28]. To make a link with experiment we simulate, in a simplified way, the STM images by calculating the integrated local density of states (ILDOS) $n(\mathbf{r}, E)$ at a distance of 1.5 \AA from the surface according to

$$n(\mathbf{r}, E) = \sum_{E < \epsilon_{nk} < 0} |\psi_{nk}(\mathbf{r})|^2, \quad (1)$$

where the summation is performed over all electron states with energies ϵ_{nk} belonging to the energy window between E and the top of the valence band (taken as the zero energy). The current in STM measurements is proportional to the ILDOS defined above. In this way, different voltages applied in STM measurements are modeled by different energy windows $\Delta E = -E$. A negative value of E implies that we sum over the occupied valence states, which corresponds to the voltage polarization used in Ref. [8]. The results obtained for PbSe(001) are displayed in Fig. 8, which shows the voltage dependence of STM images. Qualitatively, Fig. 8 reproduces the effect presented in Fig. S3 of Ref. [8], particularly the fact that different atoms are dominant under different STM voltages. In general the anions are more visible because, due to rumpling, the cations are placed deeper in the crystal. However, as expected, the STM images of the symmetric PbSe(001) surface are symmetric as well, and the maxima of the ILDOS $n(\mathbf{r}, E)$ are above the ions.

The simulated STM images change when the surface symmetry is broken, and a relative displacement of the cation and anion sublattices at the surface is assumed. In this case, calculations performed for several surface configurations reveal an interesting effect illustrated in Fig. 9. The images are obtained assuming a lateral displacement of Se in the first ML by $(0.1, 0.1) \text{ \AA}$, and the Se position is shown by a star. On the other hand, the calculated maxima of the electron density occur at approximately $(0.3, 0.3) \text{ \AA}$ in the case of very thin slabs of 5 and 9 ML. This result shows that the experimental STM images do not always directly reflect the

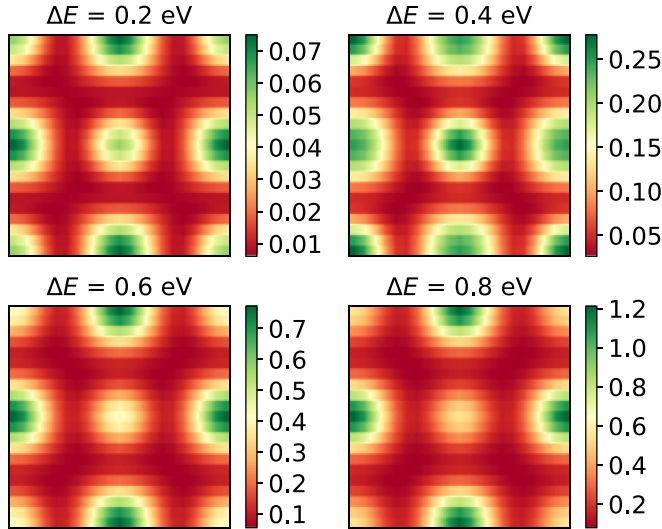


FIG. 8. Integrated local density of states $n(\mathbf{r}, E)$ at 1.5 \AA from the PbSe(001) surface calculated for a varying energy window ΔE counted from the top of the valence band (see text). The plots display a surface unit cell of dimensions $a_0 \times a_0$. Pb cations are located at the center and at the corners of the unit cell, and Se anions are in the middle of its edges.

location of atoms at the surface. However, for thicker slabs the effect disappears. Because in Ref. [8] the surface of the bulk crystal was studied, STM maxima reflect real positions of atoms. (We mention here that the sensitivity of the PbTe band gap to the slab thickness discussed in Ref. [29] showed pronounced irregularities for a few monolayer slabs. Also, in

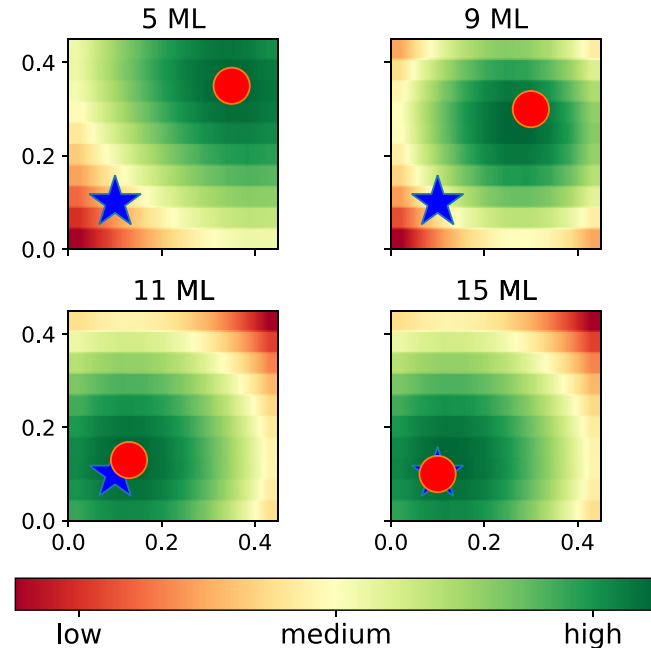


FIG. 9. ILDOS at a distance of 1.5 \AA from the PbSe(001) surface near the displaced Se atom for $E = -0.6 \text{ eV}$. Δx and Δy describe distances relative to the position of the Se atom in the perfect RS structure. The actual position of Se is denoted by the blue star, and the maximum of the calculated electron density occurs at the red circle.

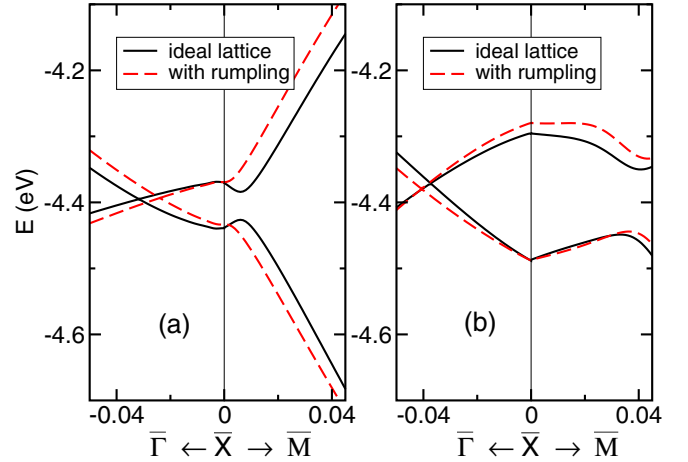


FIG. 10. The influence of rumpling on the energy bands for (a) PbTe with lattice parameter $a_0 = 6.24 \text{ \AA}$ when PbTe is in the TCI phase and (b) RS-SnSe with $a_0 = 6.105 \text{ \AA}$. In both panels only the two surface states present in the band gap are shown. The wave vector on the x axis along both the $\bar{X} \rightarrow \bar{\Gamma}$ and $\bar{X} \rightarrow \bar{M}$ directions is in units of $2\sqrt{2}\pi/a_0$.

general atomic configurations suggested by the STM images do not necessarily reflect the actual ones. For example, at the Si(001) surface the apparent tilt of Si dimers is different for positive and negative biases [30].)

C. Dispersion relations of surface states: Influence of rumpling

Surface states of the considered systems are affected both by rumpling and by chemical disorder present in alloys. The latter destroys the reflection symmetry with respect to the $\{110\}$ planes. We focus on the two surface states present in the band gap because we are interested mainly in the position of the Dirac cross and the energy gap in the vicinity of the \bar{X} point. Dispersion relations for 133 and 173 ML thick slabs and for $[110]$ and $[\bar{1}\bar{1}0]$ directions are identical.

Figure 10 compares dispersion relations for the surfaces of both PbTe and RS-SnSe with and without rumpling. The calculations for RS-SnSe are done only for comparison because, as we already mentioned, the RS phase of SnSe is not stable. In the case of PbTe, the assumed lattice parameter is 6.24 \AA , for which the compound is in the TCI phase. We see that the rumpling does not lead to opening of the gap at the Dirac cross because the reflection symmetry with respect to the $\{110\}$ planes is not broken. There are two effects induced by rumpling in the vicinity of the \bar{X} point, namely, a displacement of the Dirac cross and a change in the energy gap in the \bar{X} - \bar{M} direction. Both effects are very small. For RS-SnSe we also observe these two effects; however, compared to PbTe, the shift of the Dirac cross is of opposite sign, and the energy gap becomes larger. Like in the case of PbTe, both effects are small.

D. Bulk chemical disorder

In a pure compound like PbSe, the transition from the trivial NI to the TCI phase can be induced by hydrostatic pressure.

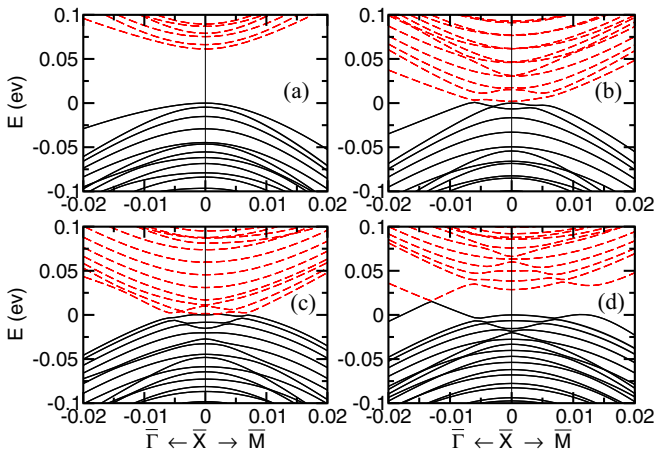


FIG. 11. Dispersion relations along the $\bar{\Gamma}$ - \bar{X} and \bar{X} - \bar{M} directions for $\text{Pb}_{1-x}\text{Sn}_x\text{Se}$ with different tin contents: (a) $x = 0.15$, (b) $x = 0.20$, (c) $x = 0.25$, and (d) $x = 0.30$. The scales for x axes are in units of the distance between the $\bar{\Gamma}$ and \bar{X} points.

Since hydrostatic pressure does not change the crystal symmetry, the states at the four L points in the Brillouin zone are degenerate for all values of the lattice constant. Consequently, the transition is sharp, and the band gap changes sign at a well-defined value of a_0 .

In alloys, chemical disorder makes the NI-TCI transition more complex. This is because the disorder splits degenerate bands (or it broadens electronic states), and as a consequence, the pressure-induced NI-TCI transition is smeared out; that is, it occurs within a finite window of hydrostatic pressures. In an analogous way, the NI-TCI transition can be induced by changing the chemical composition x of an alloy, but again, the band smearing results in a finite composition window in which the band gap vanishes. This was discussed for bulk crystals in Refs. [24,31]. Moreover, it was shown in Ref. [31] that in the transition region the alloy is in the Weyl semimetal (WSM) phase. Our calculations show that $\text{Pb}_{1-x}\text{Sn}_x\text{Se}$ is in the WSM phase for $0.18 < x < 0.30$, which is close to the window $0.12 < x < 0.30$ obtained in Ref. [31].

In Fig. 11 we present dispersion relations for the $\text{Pb}_{1-x}\text{Sn}_x\text{Se}$ 173 ML thick slab with different compositions x and random cation distributions in the supercell. For the lowest content of Sn, $x = 0.15$ [Fig. 11(a)], the crystal is in the NI phase, and the band gap is positive. Detailed analysis shows the splitting of the two lowest conduction and two highest valence bands at the \bar{X} point. This is a consequence of the chemical disorder, and in the case of pure PbSe such splitting is absent. When $x = 0.3$ [Fig. 11(d)], the crystal is in the TCI phase, and accordingly, the Dirac cross is seen.

Finally, for two intermediate concentrations, $x = 0.20$ and $x = 0.25$ [Figs. 11(b) and 11(c)], the highest valence bands and the lowest conduction bands overlap in a finite energy interval of a few meV in the vicinity of the \bar{X} point, reflecting the impact of the chemical disorder. This is interpreted as a manifestation of the WSM bulk phase [24,31].

IV. CONCLUSIONS

The presence and the form of metallic helical Dirac states critically depend on the symmetry of not only a bulk crystal

but also its surfaces. Here, we studied the properties of the (001) surfaces of PbTe, PbSe, SnTe, and SnSe, as well as the $\text{Pb}_{1-x}\text{Sn}_x\text{Se}$ substitutional alloy, and paid attention to the possible interplay between the topological TCI phase and the surface geometry. Realistic allocations of atoms in the first few monolayers at the (001) surface were determined by first-principles calculations. Equilibrium geometries of all the considered surfaces were typical of the RS crystal family. First, the rumpling takes place; that is, cations and anions from the same atomic plane are displaced from the ideal RS sites in the z direction perpendicular to the surface. In contrast, ionic displacements in the (x, y) plane of the surface are absent, and therefore, the RS surface symmetry is not broken, and close to the surface, the interlayer distances weakly oscillate. Those features are in agreement with a number of experimental data and theoretical results regarding surface geometries of the IV-VI family and other RS crystals. As these effects do not break the mirror plane symmetry of the RS(001) surfaces, their sole impact on the band structure is to shift the positions of the Dirac points, and the opening of the band gap in the spectrum of surface states does not occur. In most cases, the effect of the surface relaxation on the band energies is small, of the order of a few meV. The RS symmetry is present also in our simulated STM images of the studied surfaces. On the other hand, spontaneous symmetry breaking at the (001) surface, accompanied by the band gap opening (destruction of the Dirac cones and acquisition of mass by surface electrons), was recently reported for $\text{Pb}_{1-x}\text{Sn}_x\text{Se}$ [8] and $\text{Pb}_{1-x}\text{Sn}_x\text{Te}$ [19].

The above discrepancy between experiment and theory requires a comment. Typically, surface reconstructions stem from a specific coordination of surface atoms. An example is the formation of dimers at {001} surfaces of zinc-blende crystals. An unexpected reconstruction (which we may possibly deal with here) can take place because the film, assumed to be in, e.g., the RS phase, acquires a different crystal structure. Indeed, during the pseudomorphic growth an overlayer adopts the structure of the substrate. When the two structures differ, at some conditions (defined by the critical values of thickness, composition, or temperature) the ground state phase of the overlayer overcomes pseudomorphic constraints, and the overlayer changes structure. Clearly, this results in a change in the atomic configurations at the surface as well. In this respect we note that the equilibrium structure of SnSe and $\text{Pb}_{1-x}\text{Sn}_x\text{Se}$ ($x > 0.4$) is orthorhombic [32,33], in which phase the (001) surface can acquire the reconstruction pattern claimed in [8] (see Fig. 1 in Ref. [34]). This suggests that a possible source of the observed reconstruction is the onset of the structural bulk instability signaled at the surface. However, one should keep in mind that the observed symmetry breaking is limited to only the surface since, otherwise, the band gap would strongly differ from that measured [8].

Second, breaking mirror symmetry leads to the formation of surface dipoles [19]. This leads to yet another question regarding the surface configuration: experiment reveals only one direction of polarization, while one would expect formation of surface domains with orthogonal orientations of polarization.

Third, in the case of $\text{Pb}_{1-x}\text{Sn}_x\text{Se}$ the details of the reconstruction were directly displayed by the STM images [8]. One can observe, however, an interesting feature in Fig. S3 of

Ref. [8]. Namely, the reconstruction pattern depends on the STM polarization voltage: at about -250 mV the symmetry breaking mirror plane is (100), which changes to the (110) plane at higher voltages. This effect was not recognized by the authors and is not reflected in our calculations. Finally, we cannot propose a source of this contradiction. The above remarks are meant to underline the complexity of the issue, not to question the quoted experimental data.

To study dispersion relations of surface states we used the tight-binding approach, with parameters obtained from the DFT calculations. As we demonstrated, it is important to account for the position dependence of the TBA parameters (which differ for ions in the bulk and near the surface) since the energies of surface states are otherwise erroneous. In particular, we analyzed the transition from the NI to the TCI phase for $\text{Pb}_{1-x}\text{Sn}_x\text{Se}$. With increasing Sn content the

alloy undergoes the transition from a normal insulator to the Weyl semimetal phase. Because of the disorder-induced band broadening, this phase persists in a wide composition window, $0.2 < x < 0.3$, in which surface states are characterized by atypical dispersion relations as well as semilocalization at the surface, and eventually, the TCI phase appears for $0.3 < x < 0.4$.

ACKNOWLEDGMENTS

This work was partially supported by National Science Centre (Poland) Projects No. UMO-2016/23/B/ST3/03725 (A.Ł.) and No. UMO-2017/27/B/ST3/02470 (A.Ł.) and by the Foundation for Polish Science through the IRA Programme cofinanced by the European Union within SG OP (T.S.). We thank R. Buczko for helpful discussions.

-
- [1] G. Nimtz and B. Schlicht, in *Narrow-Gap Semiconductors*, edited by G. Höhler, Springer Tracts in Modern Physics, Vol. 98 (Springer, Berlin, 1983), pp. 1–117.
- [2] *Lead Chalcogenides: Physics and Applications*, edited by D. R. Khoklov (Taylor and Francis, New York, 2003).
- [3] T. H. Hsieh, H. Lin, J. Liu, W. Duan, A. Bansil, and L. Fu, *Nat. Commun.* **3**, 982 (2012).
- [4] P. Dziawa, B. J. Kowalski, K. Dybko, R. Buczko, A. Szczerbakow, M. Szot, E. Łusakowska, T. Balasubramanian, B. M. Wojek, M. H. Berntsen, O. Tjernberg, and T. Story, *Nat. Mater.* **11**, 1023 (2012).
- [5] Y. Tanaka, Z. Ren, T. Sato, K. Nakayama, S. Souma, T. Takahashi, K. Segawa, and Y. Ando, *Nat. Phys.* **8**, 800 (2012).
- [6] S.-Y. Xu *et al.*, *Nat. Commun.* **3**, 1192 (2012).
- [7] Y. Okada, M. Serbyn, H. Lin, D. Walkup, W. Zhou, C. Dhital, M. Neupane, S. Xu, Y. J. Wang, R. Sankar, F. Chou, A. Bansil, M. Z. Hasan, S. D. Wilson, L. Fu, and V. Madhavan, *Science* **341**, 1496 (2013).
- [8] I. Zeljkovic, Y. Okada, M. Serbyn, R. Sankar, D. Walkup, W. Zhou, J. Liu, G. Chang, Y. J. Wang, M. Z. Hasan, F. Chou, H. Lin, A. Bansil, L. Fu, and V. Madhavan, *Nat. Mater.* **14**, 318 (2015).
- [9] B. M. Wojek, M. H. Berntsen, V. Jonsson, A. Szczerbakow, P. Dziawa, B. J. Kowalski, T. Story, and O. Tjernberg, *Nat. Commun.* **6**, 8463 (2015).
- [10] B. M. Wojek, P. Dziawa, B. J. Kowalski, A. Szczerbakow, A. M. Black-Schaffer, M. H. Berntsen, T. Balasubramanian, T. Story, and O. Tjernberg, *Phys. Rev. B* **90**, 161202(R) (2014).
- [11] A. A. Lazarides, C. B. Duke, A. Paton, and A. Kahn, *Phys. Rev. B* **52**, 14895 (1995).
- [12] A. Satta and S. de Gironcoli, *Phys. Rev. B* **63**, 033302 (2000).
- [13] V. L. Deringer and R. Dronskowski, *J. Phys. Chem. C* **120**, 8813 (2016).
- [14] V. L. Deringer and R. Dronskowski, *ChemPhysChem* **14**, 3108 (2013).
- [15] S. Sawada and K. Nakamura, *J. Phys. C* **12**, 1183 (1979).
- [16] J. Ma, Y. Jia, E. Liang, L. Wu, F. Wang, X. Wang, and X. Hu, *Surf. Sci.* **551**, 91 (2003).
- [17] E. J. W. Verwey, *Recl. Trav. Chim. Pays-Bas* **65**, 521 (1946).
- [18] C. Yan, J. Liu, Y. Zang, J. Wang, Z. Wang, P. Wang, Z.-D. Zhang, L. Wang, X. Ma, S. Ji, K. He, L. Fu, W. Duan, Q.-K. Xue, and X. Chen, *Phys. Rev. Lett.* **112**, 186801 (2014).
- [19] T. Nishijima, T. Watanabe, H. Sekiguchi, Y. Ando, E. Shigematsu, R. Ohshima, S. Kuroda, and M. Shiraishi, *Nano Lett.* **23**, 2247 (2023).
- [20] OpenMX, <http://www.openmx-square.org>.
- [21] D. M. Ceperley and B. J. Alder, *Phys. Rev. Lett.* **45**, 566 (1980).
- [22] J. P. Perdew and A. Zunger, *Phys. Rev. B* **23**, 5048 (1981).
- [23] A. Łusakowski, P. Bogusławski, and T. Radzyński, *Phys. Rev. B* **83**, 115206 (2011).
- [24] A. Łusakowski, P. Bogusławski, and T. Story, *Phys. Rev. B* **98**, 125203 (2018).
- [25] T. Kendelewicz, Jr., P. Liu, G. E. Brown, Jr., and E. J. Nelson, *Surf. Sci.* **395**, 229 (1998).
- [26] K. L. I. Kobayashi, Y. Kato, Y. Katayama, and K. F. Komatsubara, *Phys. Rev. Lett.* **37**, 772 (1976).
- [27] F. Wei, C.-W. Liu, D. Li, C.-Y. Wang, H.-R. Zhang, J.-R. Sun, X. P. A. Gao, S. Ma, and Z. Zhang, *Phys. Rev. B* **98**, 161301(R) (2018).
- [28] J. Tersoff and D. R. Hamann, *Phys. Rev. B* **31**, 805 (1985).
- [29] D. Bassanezi, E. O. Wrasse, and T. M. Schmidt, *Mater. Res. Express* **5**, 015051 (2018).
- [30] P. Bogusławski, Q.-M. Zhang, Z. Zhang, and J. Bernholc, *Phys. Rev. Lett.* **72**, 3694 (1994).
- [31] Z. Wang, Q. Liu, J.-W. Luoc, and A. Zunger, *Mater. Horiz.* **6**, 2124 (2019).
- [32] A. Szczerbakow and H. Berger, *J. Cryst. Growth* **139**, 172 (1994).
- [33] M. Neupane, S.-Y. Xu, R. Sankar, Q. Gibson, Y. J. Wang, I. Belopolski, N. Alidoust, G. Bian, P. P. Shibayev, D. S. Sanchez, Y. Ohtsubo, A. Taleb-Ibrahimi, S. Basak, W.-F. Tsai, H. Lin, T. Durakiewicz, R. J. Cava, A. Bansil, F. C. Chou, and M. Z. Hasan, *Phys. Rev. B* **92**, 075131 (2015).
- [34] K. Adouby, C. Perez-Vicente, and J. C. Jumas, *Z. Kristallogr.* **213**, 343 (1998).